Axial compressive behaviour of rectangular DCFSST stub columns

You-Fu Yang[a,*], Yu-Qin Zhang[a], Feng Fu[b]

[a] *State Key Laboratory of Coastal and Offshore Engineering, Dalian University of Technology, Dalian, 116024, China*

[b] *Department of Engineering, School of Science & Technology, City, University of London, Northampton Square, London, UK*

Abstract: In this paper, a new type of rectangular double-opening concrete filled sandwich steel tube (DCFSST) is developed. This new type of composite section can keep the inner steel tubes away from the cross-sectional centroid axis through the reasonable configuration. In order to assess the structural behaviour of rectangular DCFSST members, a pilot research on stub columns under axial compression was conducted. A total of 10 specimens, including 5 with double steel square hollow sections (SHSs) and 5 with double steel circular hollow sections (CHSs), were tested with the various offset rate of inner tube (e_0) and opening ratio (ϕ). The experimental observations indicate that, generally, e_0 and ϕ have moderate effect on the failure process and failure modes of the specimens, and the failure modes of the specimens include outward local buckling of outer tube, crushing of the sandwiched concrete and inward local buckling of inner tubes. In addition, ϕ has significant influence on the load-deformation curves, axial capacity and axial compressive stiffness of the specimens; however, e_0 has no obvious effect on the above performance. Moreover, nonlinear finite element (FE) simulation on the behaviour of axially compressed rectangular DCFSST stub columns was carried out using the ABAQUS software, and the typical performance of new composite members was further analyzed by the verified FE model. Finally, the formulae to calculate the axial capacity of rectangular DCFSST stub columns were also developed based on the FE simulation results and test results.

Key Words: DCFSST stub columns; Rectangular section; Axial compression; Tests; FE model; Simplified formulae

*Corresponding author. Tel.: 86-411-8470 8510; Fax: 86-411-8467 4141.
E–mail address: youfuyang@163.com (Dr. You-Fu Yang).

1. Introduction

Concrete filled double-skin steel tube (CFDST) is manufactured by replacing the concrete near the centroid axis of cross section of traditional concrete filled steel tube (CFST) with a steel tube, and in addition to the advantages over the traditional CFST in the structural performance, the CFDST also has the characteristics of more extended cross-section, larger flexural stiffness, lighter self-weight and better seismic performance [1, 2]. As a result, the CFDSTs have potential applications in buildings, bridges and marine structures. However, for the members or structures that need to be porous functionally, withstand heavy loads, and require high stiffness and stability concurrently, such as the giant columns for super high-rise building, the tower columns of bridge or space structure, the piers in a deep valley or the deep sea, and the subsea tunnel or deep sea suspension tunnel, traditional CFST and CFDST members cannot be used or can only be used after considering complex structural measures [3-5].

In view of the abovementioned situation, on the basis of traditional rectangular CFDST with both inner and outer tube of steel rectangular hollow section (RHS) [6-11], a new type of composite member, rectangular double-opening concrete filled sandwich steel tube (DCFSST), composed of an outer steel RHS, two symmetrically distributed inner steel square hollow sections (SHSs)/circular hollow sections (CHSs) and the concrete between them, is proposed in this paper. Typical configuration of rectangular DCFSST members is demonstrated in Fig. 1. Compared with the rectangular CFDST, the inner tubes of the rectangular DCFSST are further away from the cross-sectional centroid axis, which results in a larger bending resistance. Simultaneously, replacing one larger inner tube with two smaller ones to form a rectangular DCFSST member has the effect of 'breaking up the whole into parts', and thus reducing the cost of transportation, processing and construction of the inner tubes. Furthermore, the sizes and position of both inner tubes can be adjusted to meet different stress conditions while the outer steel RHS kept invariant. For example, the sizes of the inner tube in the tension zone can be increased while the sizes of the inner tube in the compression zone can be reduced simultaneously when the member is mainly subjected to flexural loading.

Currently, the structural behaviour of rectangular CFST members have been comprehensively studied by worldwide research organizations [12-14], and the design approaches have also been given in the relevant regulations, e.g. EN 1994-1-1 [15], ANSI/AISC 360-16 [16] and GB/T 51446-2021 [17]. At the same time, experimental study and numerical simulation on static property of rectangular CFDST (containing section with outer stainless-steel tube) short members, beams and slender members were performed by a few researchers [6-11], and the corresponding approaches for axial capacity calculation were also proposed [6, 10, 11]. The results showed that, the void ratio of CFDST was an important parameter to be considered in the experiment, and reasonable simplified formulae for axial capacitycalculation of CFDST members could be obtained based on the method for traditional CFST considering of the influence of the void ratio. Moreover, Guo et al. [18] carried out tests on the performance of square CFST stub columns with two inner small size steel SHSs/CHSs, and developed the formulae for strength calculation of this kind of composite members.

According to above description, it is noticeable that the study on the structural performance of the rectangular DCFSST members is still rare, which indicates that a fundamental investigation is needed in this area to provide reference for further research and engineering application. As a result, this paper attempts to primarily study the static performance of the rectangular DCFSST stub columns subjected to axial compression, which can become the basis for the investigation into the performance of this new type of composite members under flexure and compression-flexure. The main purpose of the research includes three aspects: first, to present experimental results of 10 axially compressed rectangular DCFSST stub columns with various cross-section of inner tubes, offset rate of inner tube and opening ratio; then, to numerically simulate the axial compressive behaviour of the rectangular DCFSST stub columns and further reveal the failure mechanism of such a kind of composite members; and finally, to propose the simplified formulae for axial capacity calculation of the rectangular DCFSST stub columns under axial compression.

2. Experimental investigation

2.1. Details of the specimens

Ten rectangular DCFSST stub columns, containing 5 specimens with double steel SHSs and 5 specimens with double steel CHSs, were prepared to conduct axial compressive tests, and two inner tubes in one specimen were of the same sizes. The cross-sectional dimensions of the specimens are demonstrated in Fig. 2, where, D_{o} and B_{o} are overall depth and breadth of outer steel RHS respectively, D_{i} is overall width or diameter of inner steel SHS or CHS respectively, t_{o} and t_{i} are wall thickness of the tubes, and d_{e} is distance between the centroid of two inner steel tubes about the major axis of section. Moreover, the height (H) to breadth (B_{o}) ratio of all specimens was identical and set to be 4.0.

The experiment was mainly aimed to investigate the influence of two parameters, namely offset rate of inner tube (e_0) and opening ratio (ϕ), and the definition of them is as follows:

$$e_0 = \frac{d_{\mathrm{e}}}{D_{\mathrm{o}}} \tag{1}$$

$$\phi = \sqrt{\frac{\sum_{i=1}^{2} A_{\mathrm{si},i}}{A_{\mathrm{ce}}}} = \begin{cases} \sqrt{2B_{\mathrm{i}}^2/[(D_{\mathrm{o}}-2t_{\mathrm{o}})(B_{\mathrm{o}}-2t_{\mathrm{o}})]} & \text{(with double steel SHSs)} \\ \sqrt{1.57B_{\mathrm{i}}^2/[(D_{\mathrm{o}}\text{-}2t_{\mathrm{o}})(B_{\mathrm{o}}\text{-}2t_{\mathrm{o}})]} & \text{(with double steel CHSs)} \end{cases} \tag{2}$$

where, $A_{\mathrm{si},i}$ is the cross-sectional area of the ith inner steel tube, and A_{ce} is the cross-sectional area enclosed by the internal wall of the outer steel RHS.

The information of the test specimens is listed in Table 1, in which $N_{\mathrm{u,e}}$ and $N_{\mathrm{u,fe}}$ are the experimental axial capacity and the simulated axial capacity by finite element (FE) model described later respectively, and K_{e} is axial compression stiffness of the specimens.

The outer steel RHS was manufactured by the cold form processing of the plate and had one straight butt weld, whilst the inner tubes were cut from the finished cold-formed steel SHS or CHS. Each specimen had two endplates with side lengths slightly larger than those of the outer tube and thickness of 20 mm. Before casting the concrete, the first endplate was simultaneously welded to the end of outer and inner tubes using fillet weld, and the welding of the second endplate was conducted after curing the sandwiched concrete for 14 days. It should be noted that, to ensure reliable connection between the inner tubes and the second endplate, two holes with the same cross-section as the inner tubes were drilled at the position of the inner tubes, and a groove for peripheral fillet weld was made in advance at the opening of the endplate. Moreover, eight stiffeners were arranged between each endplate and the external wall of the outer tube to avoid the end damage of the specimens during the loading process.

2.2. Material properties

The properties of each type of steel tube were acquired through axial tension testing of three standard plate coupons. The coupons along the length direction of steel RHS/SHS were taken from the flat portion, while the coupons along the length direction of steel CHS were selected randomly. Table 2 presents the measured properties of steel sections, in which, f_{y} and f_{u} are the yield and tensile strength, E_{s} and μ_{s} are the elastic modulus and Poisson's ratio, and δ is the elongation after fracture.

The design strength grade of the sandwiched concrete was C40 (i.e. standard cubic compressive strength of 40 MPa). The materials for producing concrete included: ordinary Portland cement (P.O 42.5), fly ash (Grade I), coarse aggregate having particle size between 5 mm and 10 mm, river sand and polycarboxylic acid series of high-performance water reducer. Table 3 presents the mix proportion and properties of the concrete, in which, $f_{\mathrm{cu,28}}$ and f_{cu} are the average compressive strength at 28 days and during the test of composite columns obtained by the compression tests on the cubes with a side length of 150 mm, and E_{c} is the elastic modulus acquired by the compression tests on the prisms with side lengths of 150 mm, 150 mm and 300 mm.

2.3. Test set-up and measuring point arrangement

Static loading tests of the rectangular DCFSST stub columns were carried out by a testing machine with capacity of 10000 kN. During the test, the specimen was vertically placed on the lower platen, and a load cell was placed between specimen's top endplate and the upper platen to record the applied loads. The overall axial displacements of the specimens were measured by four displacement transducers (DTs) symmetrically placed on the lower platen. The strains at specific points on the steel tubes of the specimens were measured by the strain gauges (SGs) affixed to the external wall of the steel tubes at the half-height section, and there were 24 and 20 SGs for the specimens with double steel SHSs and CHSs, respectively. The test set-up and measuring point arrangement are displayed in Fig. 3.

The displacement control approach was used to continuously apply axial compressive loads to the specimens. In the load rising phase, the increasing rate of axial displacement was 0.2 mm/min, while in the load descending stage until the end of the test, the increasing rate of axial displacement was 1.0 mm/min. Simultaneously, a camera facing the half-height on one side of the specimen was used to record the experimental phenomena and failure process. The test was terminated until the load acting on the specimens fell to 60% of its peak value.

2.4. Experimental results and discussion

2.4.1. Overall behaviour and failure modes

Careful observation of the complete video files recorded by the camera indicated that, generally, no obvious change was found in the appearance of all specimens before achieving about 75% peak load, while slight local buckling of outer steel RHS first appeared on the depth side after reaching about 75% peak load. Moreover, when the peak load was reached, the first local buckling of outer steel RHS became more obvious and the breadth side of outer steel RHS also buckled locally, accompanied by the sound of concrete crushing. Whereafter, as the axial displacement continued to increase (i.e. damage was intensified), the load on the specimen declined rapidly and became stable gradually. Meanwhile, the local buckling of outer steel RHS became more and more serious together with the possibility of new local buckling, and eventually the main local buckling at four walls and corners of outer steel RHS were connected to form a complete elliptical ring.

Fig. 4 demonstrates the overall failure mode of the specimens, where the outward local buckling on front depth side of the outer tube is marked by the continuous dashed lines. It can be seen that, generally, the range and magnitude of local buckling of the tube depth side are larger than those of the tube breadth side as the depth side of the outer steel RHS has a higher width-to-thickness ratio, and each specimen possesses a connection of primary local buckling on four sides and corners of the outer tube. At the same time, the range and magnitude of subsequent local buckling (if any) of the outer tube are weaker than those of primary local buckling, and usually cannot form the four-sided connectivity. These failure characteristics are similar to those of previous tests [6-8]. In general, the influence of offset rate of inner tube (e_0) and opening ratio (ϕ) on the overall failure mode of the specimens is not evident, and the difference in the buckling form of the outer tube is mainly caused by the material defects and fabrication deviation of the specimens.

The failure mode of the sandwiched concrete is shown in Fig. 5. It can be seen that, in general, the failure characteristics of the concrete is similar regardless of the parameters of the specimens. The sandwiched concrete is crushed and separated from its main body within local buckling area of the outer tube, and simultaneously the sandwiched concrete has no obvious damage outside the local buckling area of the outer tube.

Fig. 6 exhibits the failure mode of the inner tubes after completion of the tests. It can be seen that, generally, the inward local buckling around the half-height section of the specimens occurs in both tubes, as the possible outward local buckling of the inner tubes was stopped by the sandwiched concrete. For the rectangular DCFSST specimens with double steel SHSs, there are serious folding-shaped local buckling on all side walls of the inner tubes, which extends to the four corners of each tube. However, for the rectangular DCFSST specimens with double steel CHSs, the inward necked local buckling of the inner tubes generally perpendicular to the major axis of the cross-section is formed as the outer tube breadth side with a smaller width-to-thickness ratio leads to a stronger constraint to the sandwiched concrete, i.e. resulting in a greater lateral stresses of the sandwiched concrete on the inner tubes along major axis of the cross-section. Moreover, the offset rate of inner tube (e_0) and opening ratio (ϕ) have no obvious effect on the buckling form and position of the inner tubes.

2.4.2. Load versus displacement curves

The obtained load (N) versus axial displacement (Δ) curves are displayed in Fig. 7 by the solid lines. It can be observed that, regardless of the difference in the experimental parameters, the $N-\Delta$ curve of all specimens generally includes four stages of approximate elastic, elastic-plastic, rapid decline from the peak and final stable stage. However, compared with the specimens with double steel CHSs, the specimens with double steel SHSs have a faster load decline rate from the peak and a lower residual capacity at the final stable stage. This is mainly because the $D_{\mathrm{i}}/t_{\mathrm{i}}$ of inner steel SHSs is larger than that of inner steel CHSs, causing a lesser post-buckling capacity. Overall, the slope of approximate elastic and prophase of elastic-plastic stage on the $N-\Delta$ curves changes with the variation in the material and geometric parameters. However, the slope of the $N-\Delta$ curve before reaching the peak generally decreases with the increase of opening ratio (ϕ). This can be explained that, while ϕ is increased, the load carrying capacity increase caused by tube area increase is lower than the axial capacity decrease caused by the concrete area reduce. The peak load on the $N-\Delta$ curve is determined as axial capacity of the specimens (N_{ue}), which are summarized in Table 1.

2.4.3. Load versus strain relationship

From the start of loading until the N_{ue} is reached, typical longitudinal strain distribution of the specimens is schematically displayed in Fig. 8, where n (=N/N_{ue}) is the load level, and for the outer steel RHS and inner steel SHS, the strain of the remaining locations without SG is determined by that of axisymmetric measuring points about the centroid axis, while for the inner steel CHS, the strain of locations without SG is determined by the linear interpolation of strain at measuring points according to their arc length from the measuring points. It should be noted that, the strain distribution after reaching N_{ue} is not included as local buckling position of the outer steel RHS is not completely located at the half-height section, thus producing an irregular strain distribution. It is shown that, generally, when $n \leq 0.5$, the longitudinal strain of all steel tubes increases almost proportionally, and the strain reading of all measuring points is close, indicating that the specimen is basically in the elastic state. However, when $n > 0.5$, the strain increasing rate at each point improves significantly; however, the strain distribution is asymmetrical because of the asymmetry of the outer tube buckling position. Simultaneously, the steel RHS and SHS show a trend that the strain at the corner portion is larger than that at the side middle, that is, the load is transferred from the side middle to the corner of the steel tube after local buckling occurred, and the strain difference between corner portion and side middle increases with the increase of n, while the strain of the inner steel CHS increases almost uniformly during the loading process. In addition, the strain development of the inner steel CHS is more uniform and sufficient than that of the inner steel SHS.

The load (N) versus strain (ε) curves of typical specimens is demonstrated in Fig. 9, where the strain at all symmetric positions is averaged to one value, the tensile and compressive strains are respectively treated as positive and negative, and ε_{y} is the average yield strain of the outer and inner tubes in one specimen. It is shown that, the variation trend of $N-\varepsilon$ curves at all measuring points are generally similar, but the strain values under the same load level are different. In general, the strain at the corner portion is larger than that at the side middle, and the strain at the breadth corner is larger than that at the depth corner, indicating that the constraint of the outer steel RHS on the sandwiched concrete mainly concentrates on the breadth corner of the cross-section. It can also be observed that, the conformity between local buckling position of the steel tubes and the half-height section of the specimens directly determines the strain development after reaching N_{ue}. For example, the local buckling of the outer steel RHS and inner steel SHS of specimen S0.40-57 is almost located at the half-height section, resulting in a more adequate strain development in the post-peak stage; however, the local buckling of the outer steel RHS and inner steel CHS of specimen C0.35-48 has certain deviation from the half-height section, leading to a relatively deficient strain development during the post-peak stage. In addition, when the N_{ue} is achieved, the longitudinal strain of each measuring point is higher than ε_{y}, that is, the half-height section of all steel tubes can attain its yield state.

Fig. 10 shows the effect of parameters on the measured load (N) versus longitudinal strain (ε_{L}) curves at representative points (a, b and e) by solid lines. It can be observed that, generally, the influence of the type of inner tubes, e_0 and ϕ on the elastic stage of $N-\varepsilon_{\mathrm{L}}$ curve is not obvious. In the elastic-plastic stage, e_0 has no evident effect on the $N-\varepsilon_{\mathrm{L}}$ curve, whilst ϕ has a significant effect on the $N-\varepsilon_{\mathrm{L}}$ curve, namely ε_{L} increases with the increase of ϕ under the same load level.

This is mainly due to the fact that, the variation in e_0 only changes the distribution of materials within the cross-section and does not fundamentally change the cross-sectional characteristics. At the same time, while ϕ increased, the area of the sandwiched concrete reduces, which weakens its supporting effect on the local buckling of the outer and inner steel tubes, leading to a earlier local buckling of them. Moreover, under different parameters, there is a remarkable difference in the post-peak phase of $N-\varepsilon_\mathrm{L}$ curve, which is mainly caused by the discrepancy between the local buckling (failure) positions of the steel tubes and the location (half-height section) of the strain gauges.

2.4.4. Mechanical indicators

To investigate the relationship between the axial capacity of the specimens and their sectional strength, the axial capacity factor (F_b) is defined as follows:

$$F_\mathrm{b}=\frac{N_\mathrm{u,e}}{N_\mathrm{uso}+N_\mathrm{uc}+N_\mathrm{usi}} \tag{3}$$

where, $N_\mathrm{uso}(=f_\mathrm{yo}A_\mathrm{so})$, $N_\mathrm{uc}(=f_\mathrm{c}'A_\mathrm{c})$ and $N_\mathrm{usi}(=\sum f_{\mathrm{yi},i}A_{\mathrm{si},i})$ are the sectional strength of the outer steel tube, the sandwiched concrete and the inner steel tubes, respectively, f_yo, f_c' and $f_{\mathrm{yi},i}$ are the yield strength of the outer steel tube, the cylindrical compressive strength of concrete and the yield strength of the *i*th inner steel tube, respectively, and A_so and A_c are the cross-sectional area of the outer steel tube and the sandwiched concrete, respectively. In this paper, the provisions in the EN 1992-1-1 [19] were used to convert f_cu to f_c'.

The effect of parameters (e_0 and ϕ) on $N_\mathrm{u,e}$ and F_b of the specimens is indicated in Fig. 11(a). The results show that, F_b is generally larger than 1.0 and the average value of F_b of specimens with double steel SHSs and those with double steel CHSs equal to 1.058 and 1.024, respectively, which indicates that the steel RHS with $D_\mathrm{o}/B_\mathrm{o}=2.0$ still has constraint effect on the sandwiched concrete while the inner tubes provide reliable support. It can also be observed that, generally, a higher ϕ leads to a smaller $N_\mathrm{u,e}(F_\mathrm{b})$, considering that the decrease of the concrete area has a more obvious effect on the reduction of axial capacity. However, there is no consistent effect of e_0 on $N_\mathrm{u,e}(F_\mathrm{b})$ of the two types of specimens, as the inner tubes of the specimens generally exhibit failure by reaching the yield state, which is independent of their positions.

Referring to the approach in Yang et al. (2021) [20], axial compression stiffness (K_{e}) of the rectangular DCFSST stub columns is defined as follows:

$$K_{\mathrm{e}}=\frac{0.4N_{\mathrm{u,e}}}{\varepsilon_{\mathrm{L},0.4}} \tag{4}$$

where, $\varepsilon_{\mathrm{L},0.4}$ is the average longitudinal strain when the load in the ascending phase of the measured $N-\varepsilon_{\mathrm{L}}$ curve reaches $0.4N_{\mathrm{u,e}}$.

Simultaneously, axial compression stiffness ratio (R_{k}) is further defined to discover the relationship between K_{e} of the specimens and their sectional compressive stiffness:

$$R_{\mathrm{k}}=\frac{K_{\mathrm{e}}}{E_{\mathrm{so}}A_{\mathrm{so}}+E_{\mathrm{c}}A_{\mathrm{c}}+\sum E_{\mathrm{si},i}A_{\mathrm{si},i}} \tag{5}$$

where, E_{so}, E_{c} and $E_{\mathrm{si},i}$ are the elastic modulus of outer steel tube, the sandwiched concrete and the *i*th inner steel tube, respectively.

Fig. 11(b) demonstrates the influence of e_0 and ϕ on $K_{\mathrm{e}}(R_{\mathrm{k}})$ of the specimens. It is shown that, K_{e} and R_{k} of two types of specimens exhibit the same variation trend when the experimental parameters change, i.e., $K_{\mathrm{e}}(R_{\mathrm{k}})$ generally decreases with the increase of ϕ and e_0 has no consistent influence on $K_{\mathrm{e}}(R_{\mathrm{k}})$. These are similar to the trend in Fig. 11 (a). Moreover, R_{k} has a mean and standard deviation (SD) of 0.923 and 0.039, respectively. This means that, the axial compression stiffness (K_{e}) of rectangular DCFSST stub columns can be calculated based on the elastic modulus and area of each component, and generally the safe calculation results can be obtained.

3. Finite element (FE) simulation

3.1. General description

To better theoretically understand the axial compressive behaviour of the rectangular DCFSST stub columns, nonlinear finite element (FE) models were constructed by software ABAQUS [21].

The elastic properties of the steel tubes, including E_{s} and μ_{s}, replicated those obtained from tensile coupon tests (see Table 2). The inelastic property of the steel tubes, i.e. the relationship between true stress and plastic strain, was depicted using the metal plasticity model in the software [21]. As stated earlier, the outer steel RHS and inner steel SHSs of the specimens were cold-formed, which means that their flat and corner portion have different material properties. Therefore, the relationship between true stress and plastic strain of the flat portion in the steel RHS and SHSs was acquired by transforming the engineering stress (σ_s) versus engineering strain (ε_s) relationship in [22], as indicated in Eq. (6a). At the same time, the $\sigma_s - \varepsilon_s$ relationship of corner portion of the steel RHS and SHSs was same as that of flat portion; however, a higher yield strength for the corner portion was determined according to the ratio of corner radius to thickness and the ratio of tensile strength to yield strength of flat portion [22]. In the FE modelling, the approach for determing the weighted-average yield strength and the corner radius of the cold-formed steel RHS as well as SHSs in [23] and [24] was employed, respectively. In addition, for the inner steel CHSs, the true stress versus plastic strain relationship was acquired by transforming the $\sigma_s - \varepsilon_s$ relationship including five segments in [20], as indicated in Eq. (6b). In order to simplify the numerical simulation reasonably and ensure its convergence, both endplates of the specimens were ignored, and the boundary conditions were applied to the same plane of steel tubes and the sandwiched concrete.

$$\sigma_{\mathrm{s}} = \begin{cases} E_{\mathrm{s}}\varepsilon_{\mathrm{s}} & (\varepsilon_{\mathrm{s}} \le \varepsilon_{\mathrm{a}}) \\ f_{\mathrm{p}} + E_{\mathrm{s1}}(\varepsilon - \varepsilon_{\mathrm{e}}) & (\varepsilon_{\mathrm{a}} < \varepsilon_{\mathrm{s}} \le \varepsilon_{\mathrm{b}}) \\ f_{\mathrm{ym}} + E_{\mathrm{s2}}(\varepsilon - \varepsilon_{\mathrm{e1}}) & (\varepsilon_{\mathrm{b}} < \varepsilon_{\mathrm{s}} \le \varepsilon_{\mathrm{c}}) \\ f_{\mathrm{y}} + E_{\mathrm{s3}}(\varepsilon - \varepsilon_{\mathrm{e1}}) & (\varepsilon_{\mathrm{s}} > \varepsilon_{\mathrm{c}}) \end{cases} \tag{6a}$$

where, $f_{\mathrm{p}} = 0.75 f_{\mathrm{y}}$, $f_{\mathrm{ym}} = 0.875 f_{\mathrm{y}}$, $E_{\mathrm{s1}} = E_{\mathrm{s}}/2$, $E_{\mathrm{s2}} = E_{\mathrm{s}}/10$, $E_{\mathrm{s3}} = E_{\mathrm{s}}/200$, $\varepsilon_{\mathrm{a}} = 0.75 f_{\mathrm{y}}/E_{\mathrm{s}}$, $\varepsilon_{\mathrm{b}} = \varepsilon_{\mathrm{a}} + 0.125 f_{\mathrm{y}}/E_{\mathrm{s1}}$, and $\varepsilon_{\mathrm{c}} = \varepsilon_{\mathrm{b}} + 0.125 f_{\mathrm{y}}/E_{\mathrm{s2}}$.

$$\sigma_{\mathrm{s}} = \begin{cases} E_{\mathrm{s}}\varepsilon_{\mathrm{s}} & (\varepsilon_{\mathrm{s}} \le \varepsilon_{\mathrm{e}}) \\ -A\varepsilon_{\mathrm{s}}^2 + B\varepsilon_{\mathrm{s}} + C & (\varepsilon_{\mathrm{e}} < \varepsilon_{\mathrm{s}} \le \varepsilon_{\mathrm{y}}) \\ f_{\mathrm{y}} & (\varepsilon_{\mathrm{y}} < \varepsilon_{\mathrm{s}} \le \varepsilon_{\mathrm{n}}) \\ f_{\mathrm{y}}\left(1 + 0.6\frac{\varepsilon_{\mathrm{s}} - \varepsilon_{\mathrm{n}}}{\varepsilon_{\mathrm{u}} - \varepsilon_{\mathrm{n}}}\right) & (\varepsilon_{\mathrm{n}} < \varepsilon_{\mathrm{s}} \le \varepsilon_{\mathrm{u}}) \\ 1.6 f_{\mathrm{y}} & (\varepsilon_{\mathrm{s}} > \varepsilon_{\mathrm{u}}) \end{cases} \tag{6b}$$

where, ε_{e}=0.8 $f_{\mathrm{y}}/E_{\mathrm{s}}$, ε_{y}=1.5ε_{e}, ε_{n}=10ε_{y}, ε_{u}=100ε_{y}, $A = 0.2 f_{\mathrm{y}}/(\varepsilon_{\mathrm{y}} - \varepsilon_{\mathrm{e}})^2$, $B = 2A\varepsilon_{\mathrm{y}}$, and $C = 0.8 f_{\mathrm{y}} + A\varepsilon_{\mathrm{e}}^2 - B\varepsilon_{\mathrm{e}}$.

The elastic properties of the sandwiched concrete, including elasticity modulus and Poisson's ratio, were set to be $4730\sqrt{f_c'}$ [25] and 0.2 [26], respectively. The damaged plasticity model in the software [21] was employed to capture the inelasticity of the sandwiched concrete, in which, the isotropic compressive/tensile plasticity and isotropic damaged elasticity were assumed, and the yield and failure surface were controlled by the equivalent compressive/tensile plastic strain. The tension stiffening of the sandwiched concrete was captured through the fracture energy cracking criterion [21]. Moreover, it is noted that, the $D_{\mathrm{i}}/t_{\mathrm{i}}$ of the inner steel tubes in the rectangular DCFSST stub column specimens is lower than the limit of hollow steel tube in steel structures, and the experimental results also show that the inner steel tubes can provide reliable support for the sandwiched concrete until the axial capacity is reached, that is, the structural properties of the sandwiched concrete are consistent with the concrete core of the corresponding rectangular CFST and CFDST stub columns [6, 10, 12], i.e. the confinement effect of the outer steel RHS on the sandwiched concrete needs to be incorporated. As a result, the engineering stress (σ_{c}) versus engineering strain (ε_{c}) relationship under compression in [12, 27] was chosen to get the input data pair between compressive stress and inelastic strain of the sandwiched concrete in the rectangular DCFSST stub columns, as described in the following equations:

$$\sigma_{\mathrm{c}}/f_{\mathrm{c}}' = \begin{cases} 2(\varepsilon_{\mathrm{c}}/\varepsilon_{\mathrm{c0}}) - (\varepsilon_{\mathrm{c}}/\varepsilon_{\mathrm{c0}})^2 & (\varepsilon_{\mathrm{c}}/\varepsilon_{\mathrm{c0}} \le 1) \\ \dfrac{\varepsilon_{\mathrm{c}}/\varepsilon_{\mathrm{c0}}}{\rho\cdot(\varepsilon_{\mathrm{c}}/\varepsilon_{\mathrm{c0}}-1)^m+\varepsilon_{\mathrm{c}}/\varepsilon_{\mathrm{c0}}} & (\varepsilon_{\mathrm{c}}/\varepsilon_{\mathrm{c0}} > 1) \end{cases} \tag{7}$$

where, $\varepsilon_{\mathrm{c0}} = (1300 + 12.5f_{\mathrm{c}}' + 800\xi^{0.2})/1\mathrm{E}6$, $\rho = (f_{\mathrm{c}}')^{0.1}/(1.2\sqrt{1+\xi})$, $m = 1.5(\varepsilon_{\mathrm{c0}}/\varepsilon_{\mathrm{c}}) + 1.6$, and ξ is the nominal confinement factor [6].

All steel tubes were modelled by S4 elements having 9 integration points along the thickness, and the sandwiched concrete was simulated by C3D8R elements. In the modelling, the steel tubes and the sandwiched concrete possessed the same meshing nodes to ensure connectivity and computational efficiency. The surface-to-surface contacts were defined to reproduce the interfacial properties between steel tubes and the sandwiched concrete of the rectangular DCFSST stub columns. The 'hard contact' was considered in the normal direction, and the 'Coulomb friction' model with the friction coefficient of 0.6 [12, 28] was adopted in the tangential directions. Fig. 12 shows the meshing of the FE model.

During the FE modelling, the boundary conditions of the rectangular DCFSST stub columns subjected to axial compression are also shown in Fig. 12. In the initial step, the 'ENCASTRE' was defined as the boundary conditions of the bottom plane, that is, all degrees of freedom were restricted, and for the top plane the '$U_X=U_Y=0$' was defined, i.e. translational displacements in both directions were prevented. In the loading step, axial displacements of 40 mm were acted upon the top plane. It is noted that, for the axially compressed rectangular DCFSST stub columns, the residual stresses together with initial imperfections of steel RHS/SHSs are not included in the FE modelling according to the research outcomes presented in [28].

3.2. Validation of the FE model

Fig. 13 demonstrates the modelled failure modes of different components in typical rectangular DCFSST stub column specimens. It is shown that, generally, the simulated failure mode of the outward local buckling of the outer steel RHS (Fig. 13(a)) and the inward local buckling of the inner steel tubes (Fig. 13(c)) accords well with the experimental results (Figs. 4 and 6); however, the simulated local buckling position (around half-height section) differ from the tested one, to some extent. This is mainly because the actual conditions of the test specimens, such as the random distribution of material defects in each component, local size deviation and eccentricity of loading, cannot be effectively considered by the FE model. In addition, the results in Figs. 5 and 13(b) indicate that, both the simulated and measured failure mode of the sandwiched concrete occur in the local buckling position(s) of the steel tubes.

The comparison of load (N) versus deformation (Δ and ε) curves between the predicted and measured results is demonstrated in Figs. 7 and 10, where the capital letters P and M in parentheses following the specimen label represent the predicted and measured curve, respectively. It is shown that, with the increase of the deformations, the variation trend of the simulated load is generally consistent with that of the measured one; however, there is a certain deviation between the simulated curve and the corresponding one from the tests, including a higher slope before reaching N_{ue} and a lower slope after reaching N_{ue} of the simulated curves. This can also be explained that, the current FE model cannot reasonably consider the real conditions of the specimens mentioned above.

Fig. 14 shows the comparison between the simulated axial capacities using the FE model ($N_{\mathrm{u,fe}}$)

and the measured axial capacities ($N_{\mathrm{u,e}}$) of the axially compressed rectangular DCFSST stub column specimens in this study. The results indicate that the overall difference between $N_{\mathrm{u,fe}}$ and $N_{\mathrm{u,e}}$ is within 10%, and the mean and SD of $N_{\mathrm{u,fe}}/N_{\mathrm{u,e}}$ equal to 0.960 and 0.038, respectively. It can be found that the FE model built in this paper can better predict the axial capacity of the rectangular DCFSST stub columns under axial compression.

3.3. Analysis using the FE model

Based on the above FE model verified by the experimental observations, the axial compressive behaviour of the rectangular DCFSST stub columns is further analyzed with e_0 and ϕ as main parameters. The basic conditions of the example are as follows: $D_{\mathrm{o}} \times B_{\mathrm{o}} = 600$ mm $\times$ 300 mm, $H = 1200$ mm, $D_{\mathrm{o}}/t_{\mathrm{o}} = 54.5$ (i.e. nominal steel ratio $\alpha_{\mathrm{n}} = A_{\mathrm{so}}/A_{\mathrm{ce}} = 0.11$), $t_{\mathrm{i}} = 4$ mm, $f_{\mathrm{yo}} = f_{\mathrm{yi}} = 345$ MPa, $f_{\mathrm{c}}' = 50$ MPa, $e_0 = 0.5$, and for the columns with double steel SHSs, $\phi = 0.59$, and for the columns with double steel CHSs, $\phi = 0.53$.

Fig. 15 shows the computed $N - \varepsilon_{\mathrm{L}}$ curve of typical rectangular DCFSST stub columns under axial compression, where DS and DC in parentheses represent the columns with double steel SHSs and CHSs, respectively. It can be observed that, generally, the effect of e_0 and ϕ on the calculated $N - \varepsilon_{\mathrm{L}}$ curve is similar to the experimental results, i.e. e_0 has a moderate on the trend of the $N - \varepsilon_{\mathrm{L}}$ curve and the axial capacity (N_{u}) of the columns; however, the columns with a smaller ϕ have a larger N_{u} and a higher post-peak strength. It should be noted that, the capacity of column having double steel SHSs and $\phi = 0.82$ ($B_{\mathrm{i}}/t_{\mathrm{i}} = 58$) continued to decrease after the peak, indicating that the inner steel SHSs could not provide a stable capacity after locally buckling. Therefore, for the rectangular DCFSST columns, the attention should be paid to the matching of ϕ with $B_{\mathrm{i}}/t_{\mathrm{i}}$ of the inner steel SHSs in practical design.

The effect of ϕ on stress state of different components in the axially compressed rectangular DCFSST stub columns while reaching the axial capacity (N_{u}) is demonstrated in Fig. 16, and the results for e_0 change are not shown as its influence is moderate. It can be observed that, generally, ϕ has no obvious impact on the Mises stress distribution and values of the steel tubes, that is, the

Mises stress of flat and corner portion in the outer steel RHS as well as the inner steel SHSs reaches their yield strength, and the Mises stress of the inner steel CHSs also reaches their yield strength. Moreover, the longitudinal stresses (S33) across the section of the sandwiched concrete reach its maximum in the corner and gradually decays to the side middle, and the maximum stress is obviously higher than f_c', which is consistent with the characteristics of rectangular CFST [12]. At the same time, the S33 of the sandwiched concrete decreases with the increase of ϕ, especially for the columns with double steel CHSs.

The effect of e_0 and ϕ on interaction stress (p) between steel tube and the sandwiched concrete at the representative points is indicated in Fig. 17. It can be seen that, generally, p at the corner of the outer steel RHS (point a) is significantly higher than that at the side middle of the inner steel tubes (points b, d and f), indicating that the constraint effect of the outer tube on the concrete is obviously stronger than the supporting effect of the inner tubes. This is consistent with the S33 distribution results of the sandwiched concrete in Fig. 16. At point a, the variation of p reflects that the outer tube and concrete are stressed separately at first and contact with each other quickly until the peak attains; however, p decreases first and then increases slowly due to the local buckling of the outer tube. Furthermore, p generally decreases with the increase of e_0 and ϕ, and the effect of ϕ on p is more significant than e_0 as the change of ϕ significantly changes the volume of the sandwiched concrete. At points b, d and f, e_0 and ϕ have no consistent effect on p, which may be caused by the subtle differences in the buckling process and morphology of the inner tubes.

4. Simplified formulae for calculating the axial capacity

By investigating the FE simulation results of the test specimens and the designed examples in Figs. 13 and 16, it can be observed that, the inner steel tubes of the rectangular DCFSST stub columns under axial compression generally reach their yielding state while the axial capacity achieved, which is consistent with the previous findings [6, 20]. As a result, the yield strength of the inner steel tubes can be directly subtracted from the axial capacity of new composite columns to assess the influence of parameters on the strength of the outer tube and the sandwiched concrete, and the strength index ($f_{\mathrm{scy,d}}$) of the rectangular DCFSST stub columns under axial compression is defined as follows:

$$f_{\mathrm{scy,d}} = \frac{N_{\mathrm{u}}\text{-}\Sigma f_{\mathrm{yi},i} A_{\mathrm{sh},i}}{(A_{\mathrm{so}}+A_{\mathrm{c}})} \tag{8}$$

Furthermore, in view of the fact that the cross-sectional composition of a rectangular DCFSST is similar to that of a rectangular CFDST, as well as the similar stress state of the steel tube(s) inside them while N_{u} is reached, the strength index ratio (k) of the former and the latter is defined as:

$$k = \frac{f_{\mathrm{scy,d}}}{f_{\mathrm{scy,s}}} \tag{9}$$

in which, $f_{\mathrm{scy,s}}$ is the simplified strength index of a rectangular CFDST [6].

The effect of parameters on the strength index ratio (k) is demonstrated in Fig. 18. It can be seen that, regardless of the type of inner tubes, the k values are generally maintained around 1.0, although individual parameters (e.g. $f_{\mathrm{yo(i)}}$ and f_{c}') have a certain influence on k, that is, the simplified strength index ratio of the rectangular CFDST can be directly applied to the rectangular DCFSST.

According to Eqs. (8) and (9), the formula for the axial capacity calculation of the rectangular DCFSST stub columns can be obtained:

$$N_{\mathrm{u}} = \left[C_1\phi^2 f_{\mathrm{yo}} + C_2(1.18 + 0.85\xi)f_{\mathrm{ck}}\right](A_{\mathrm{so}} + A_{\mathrm{c}}) + \sum f_{\mathrm{yi},i}A_{\mathrm{sh},i} \tag{10}$$

where, C_1 and C_2 are the parameters related to the steel ratio and nominal steel ratio, and f_{ck} is the characteristic compressive strength of concrete [1, 6].

The comparison between the calculation results ($N_{\mathrm{u,s}}$) of Eq. (10) and the FE simulation results ($N_{\mathrm{u,fe}}$) as well as experimental results ($N_{\mathrm{u,e}}$) is respectively shown in Figs. 19 and 20, and the mean and SD of $N_{\mathrm{u,s}}/N_{\mathrm{u,fe}}$ ($N_{\mathrm{u,s}}/N_{\mathrm{u,e}}$) are 0.997 (0.955) and 0.030 (0.045), respectively. It can be found that, the calculated axial capacities of the axially compressed rectangular DCFSST stub columns using the simplified formulae are in good agreement with the FE simulation and experimental results, and the differences between the objects of comparison are generally within 10%. Based on the experimental and numerical studies in this paper, the application range of Eq. (10) is: D_{o}=300-600 mm, α_{n}=0.06-0.18, e_0=0.35-0.6; ϕ=35%-82%, f_{y}=235-460 MPa, f_{c}'=25-75 MPa, and $D_{\mathrm{i}}/t_{\mathrm{i}} <$

$[D_i/t_i]$, where $[D_i/t_i]$ is the limit of the width/diameter-to-thickness ratio of the inner steel tubes.

5. Conclusions

The axial compressive behaviour of a new type of rectangular double-opening concrete filled sandwich steel tube (DCFSST) stub column is investigated, and based on the experiments and numerical simulations in this study the following conclusions can be drawn:

(1) The observed failure modes of typical specimens show that, offset rate of inner tube (e_0) and opening ratio (ϕ) have a moderate effect on the failure modes of rectangular DCFSST stub column specimens. In general, there are 1 to 2 outward local buckling spots noticed in the various locations on outer steel RHS and the local buckling on the depth side is more obvious than that on the breadth side. Moreover, the sandwiched concrete is crushed at the buckling position of the outer tube, while both inner steel tubes buckle inwards in the crushed location of the sandwiched concrete.

(2) The relationship between load (N) and axial displacement (Δ)/strain (ε) of the specimens are recorded, and the results demonstrate that e_0 generally has little effect on the initial slope of $N-\Delta$ curve of rectangular DCFSST stub columns; however, the slope of the ascending stage of $N-\Delta$ curve decreases with the increase of ϕ, and the deformability of the specimens with double steel CHSs is better than those with double steel SHSs. The variation trend of $N-\varepsilon$ curve is generally consistent with that of $N-\Delta$ curve. Simultaneously, at the half-height section of the outer steel RHS, the strain development of side middle is slower than that of corner portion.

(3) The variation characteristics of the key mechanical indexes of the specimens are studied, and it is found that the axial capacity (N_{ue}) and axial compression stiffness (K_e) of the specimens generally decreases while ϕ increased; however, the effect of e_0 on N_{ue} and K_e is not obvious. The axial compression stiffness (K_e) of rectangular DCFSST stub columns can be safely determined by the sumation of the product of elastic modulus and area of each component.

(4) The finite element (FE) simulation is conducted, and the modelling results indicate that the constructed FE model can well reproduce the failure process and modes, load-deformation curves, axial capacity and stress state of the rectangular DCFSST stub columns under axial compression. In

addition, the interaction stress (p) at the corner of the outer steel RHS, which well reflects the change in loading state between outer tube and concrete, is much higher than that at the side middle of the inner steel tubes, and e_0 and ϕ have remarkable effect on p at the corner of the outer steel RHS.

(5) A simplified method for axial capacity calculation is suggested, and the comparison shows that the simplified formulae based on the parameter analysis results can accurately predict the axial capacity of DCFSST stub columns under axial compression, and the difference between the simplified and the FE simulation/measured results is within 10%.

It's worth noting that the rectangular DCFSST members may bear the combined action of axial forces and bending moments. As a result, further studies on the performance of rectangular DCFSST beams and beam-columns are necessary for guiding their design and application.

Declaration of Competing Interest

The authors declare that they have no known competing financial interests or personal relationships that could have appeared to influence the work reported in this paper.

Acknowledgement:

The research work reported herein was supported by the National Natural Science Foundation of China (No. 51678105). The research funding is highly appreciated. The authors also wish to thank Ms. Min Hou for her help in the tests.

References:

[1] L.H. Han, D. Lam, D.A. Nethercot, Design Guide for Concrete-Filled Double Skin Steel Tubular Structures, CRC Press, UK, 2018.

[2] L. H. Han, W. Li, R. Bjorhovde, Developments and advanced applications of concrete-filled steel tubular (CFST) structures: Members, J. Constr. Steel. Res. 100 (2014) 211-228.

[3] M.C.H. Hui, C.K.P. Wong, Stonecutters Bridge-durability, maintenance and safety considerations, Struct. Infrastruct. Eng. 5(3) (2009) 229-243.

[4] X. Lu, X. Lu, H. Guan, W. Zhang, L. Ye, Earthquake-induced collapse simulation of a super-tall mega-braced frame-core tube building, J. Constr. Steel. Res. 82 (2013) 59-71.

[5] Z.B. Wang, L.H. Han, W. Li, Z. Tao, Seismic performance of concrete-encased CFST piers: experimental study, J. Bridge Eng. 21(4) (2016) 04015072.

[6] Z. Tao, L.H. Han, Behaviour of concrete-filled double skin rectangular steel tubular beam-columns, J. Constr. Steel. Res. 62(7) (2006) 631-646.

[7] L. Xie, M. Chen, H. Huang, Experimental study on rectangular concrete-filled double-skin steel tubes subjected to axial compressive load, Industrial Construction 43(5) (2013) 128-131. (in Chinese)

[8] H. Huang, Y. Zhu, M. Chen, K. Xu, Experimental investigation on axial compression of rectangular recycled concrete-filled double-skin steel tube short column, J. Experimental Mechanics 31(1) (2016) 67-74. (in Chinese)

[9] M. Rizwan, Q.Q. Liang, M.N.S. Hadi, Numerical analysis of rectangular double-skin concrete-filled steel tubular slender columns incorporating interaction buckling, Eng. Struct. 245 (2021) 112960.

[10] M. Rizwan, Q.Q. Liang, M.N.S. Hadi, Fiber-based computational modeling of rectangular double-skin concrete-filled steel tubular short columns including local buckling, Eng. Struct. 248 (2021) 113268.

[11] M. Ahmed, Q.Q. Liang, A. Hamoda, M. Arashpour, Behavior and design of thin-walled double-skin concrete-filled rectangular steel tubular short and slender columns with external stainless-steel tube incorporating local buckling effects, Thin-Walled Struct. 170 (2022) 108552.

[12] Y.F. Yang, C. Hou, M. Liu, Tests and numerical simulation of rectangular RACFST stub columns under concentric compression, Structures 27 (2020) 396-410.

[13] Y.F. Yang, Y.Q. Zhang, F. Fu, Performance and design of RAC-filled steel RHS beams, J. Build. Eng. 46 (2022) 103734.

[14] Y. Wang, H. Lin, Z. Lai, D. Li, W. Zhou, X. Yang, Flexural behavior of high-strength rectangular concrete-filled steel tube members, J. Struct. Eng. 148(1) (2022) 04021230.

[15] EN 1994-1-1. Eurocode 4: Design of Composite Steel and Concrete Structures-Part 1-1: General Rules and Rules for Buildings, European Committee for Standardization, Brussels, Belgium, 2004.

[16] ANSI/AISC 360-16. Specification for Structural Steel Buildings, American Institute of Steel Construction (AISC), Chicago, USA, 2016.

[17] GB/T 51446-2021. Technical Standard for Concrete-Filled Steel Tubular Hybrid Structures, Beijing: China Architecture & Building Press, 2021.

[18] Z. Guo, Y. Chen, Y. Wang, M. Jiang, Experimental study on square concrete-filled double skin steel tubular short columns, Thin-Walled Struct. 156 (2020) 107017.

[19] EN 1992-1-1. Eurocode 2: Design of Concrete Structures-Part 1-1: General Rules and Rules for Buildings, European Committee for Standardization, Brussels, Belgium, 2004.

[20] Y.F. Yang, F. Fu, X.M. Bie, X. H. Dai. Axial compressive behaviour of CFDST stub columns with large void ratio, J. Constr. Steel. Res. 186 (2021) 106892.

[21] Simulia, ABAQUS Analysis User's Guide, Version 6.14, Dassault Systèmes Simulia Corp, Providence, RI, 2014.

[22] N. Abdel-Rahman, K.S. Sivakumaran, Material properties models for analysis of cold-formed steel members, J. Struct. Eng. 123(9) (1997) 1135-1143.

[23] M. Elchalakani, X.L. Zhao, R. Grzebieta, Tests on concrete filled double-skin (CHS outer and SHS inner) composite short columns under axial compression, Thin-Walled Struct. 40 (5) (2002) 415-441.

[24] AISI, North American Specification for the Design of Cold-formed Steel Structural Members, American Iron and Steel Institute (AISI), North American Standard, Washington DC, USA, 2001.

[25] ACI Committee 318, Building Code Requirements for Structural Concrete (ACI 318-19) and Commentary, American Concrete Institute, Detroit, USA, 2019.

[26] FIB, Fib Model Code for Concrete Structures 2010, Fédération Internationale du Béton, Ernst & Sohn, Berlin, Germany, 2013.

[27] L.H. Han, G.H. Yao, Z. Tao. Performance of concrete-filled thin-walled steel tubes under pure torsion, Thin-Walled Struct. 45(1) (2007) 24-36.

[28] Z. Tao, Z.B. Wang, Q. Yu, Finite element modelling of concrete-filled steel stub columns under axial compression, J. Constr. Steel. Res. 89 (2013) 121-131.

Figures:

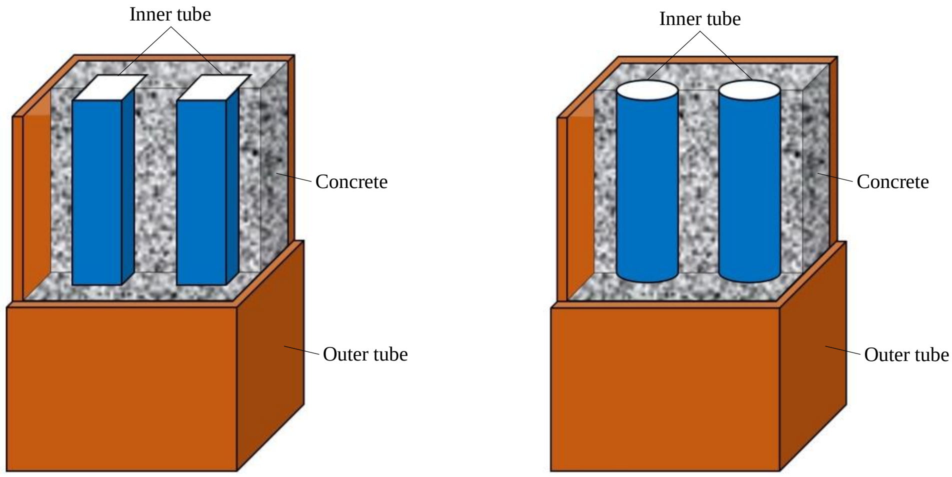

(a) With double steel SHSs (b) With double steel CHSs

Fig. 1. Typical configuration of rectangular DCFSST members.

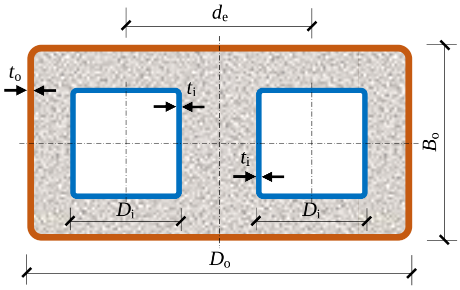

(a) Section with double steel SHSs

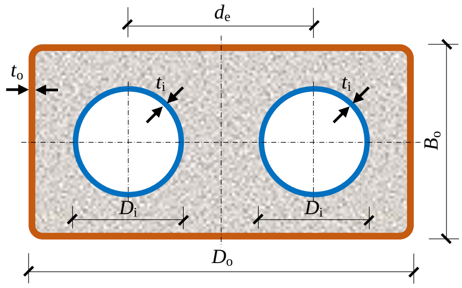

(b) Section with double steel CHSs

Fig. 2. Cross-sectional dimensions of the specimens.

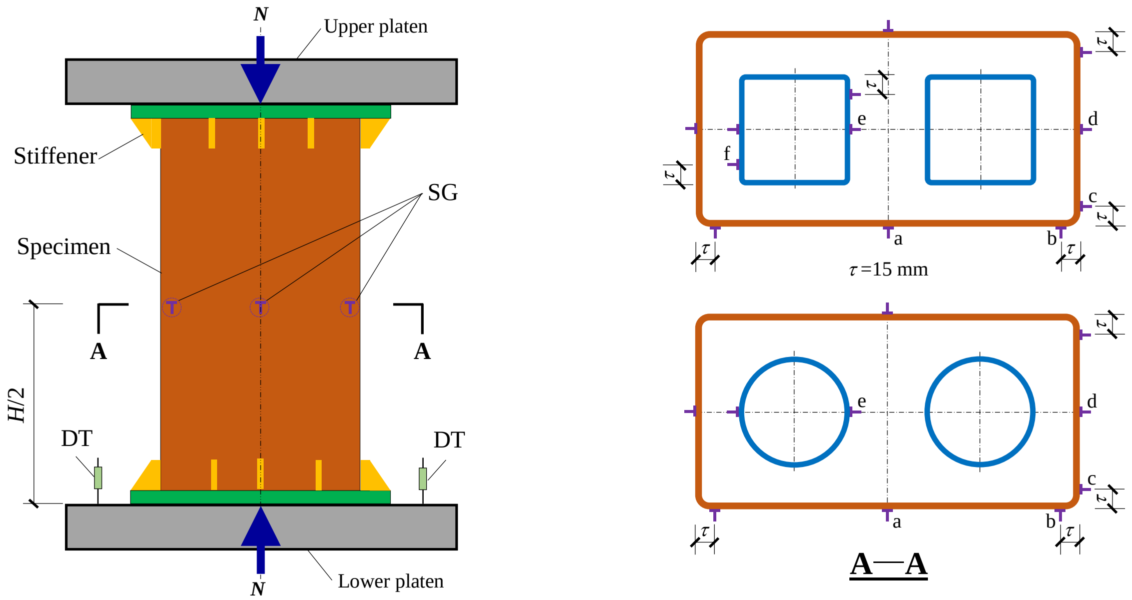

Fig. 3. Test set-up and measuring point arrangement.

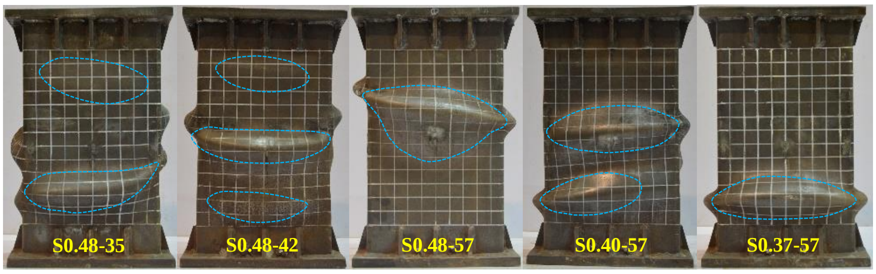

(a) With double steel SHSs

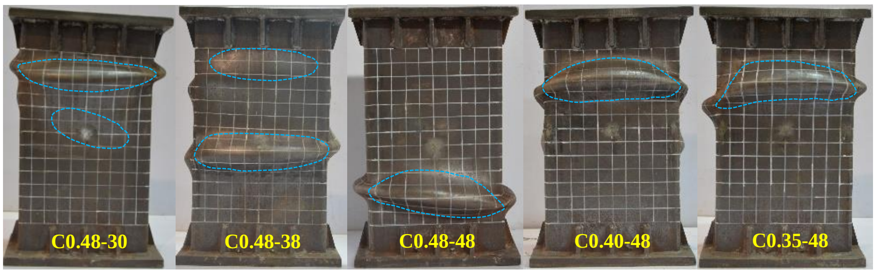

(a) With double steel CHSs

Fig. 4. Overall failure mode of the specimens.

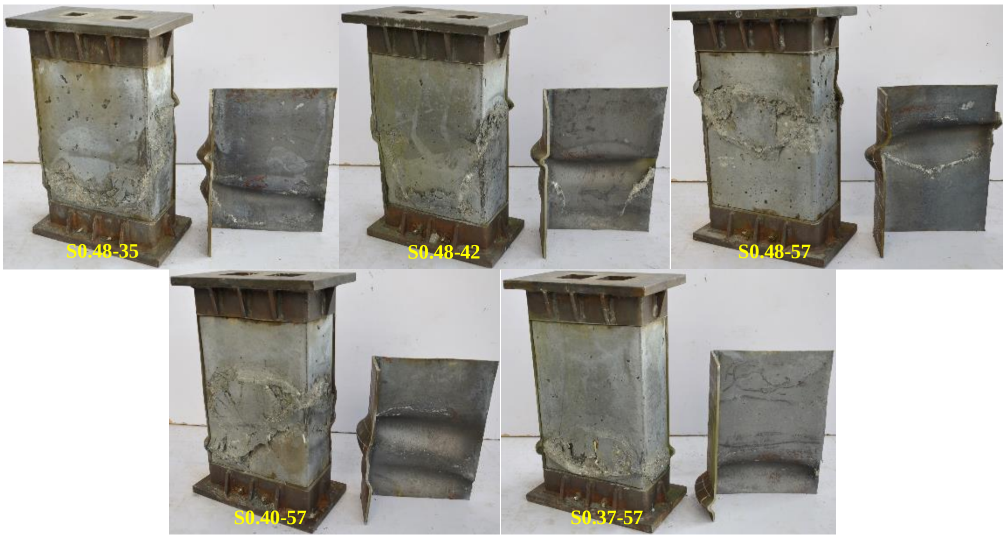

(a) With double steel SHSs

(b) With double steel CHSs

Fig. 5. Failure mode of the sandwiched concrete.

(a) With double steel SHSs

(b) With double steel CHSs

Fig. 6. Failure mode of inner tubes.

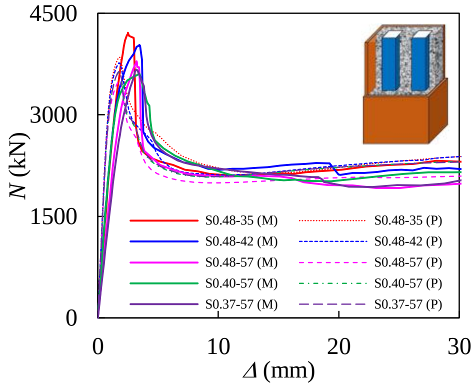

(a) With double steel SHSs

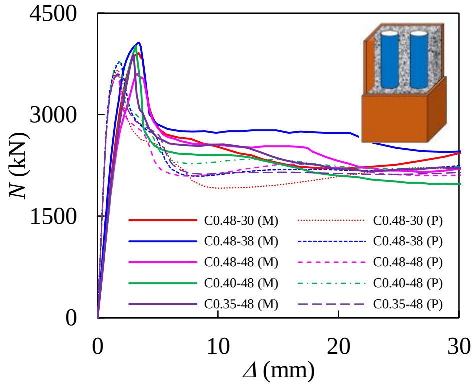

(b) With double steel CHSs

Fig. 7. Load (N) versus axial displacement (Δ) curve of the specimens.

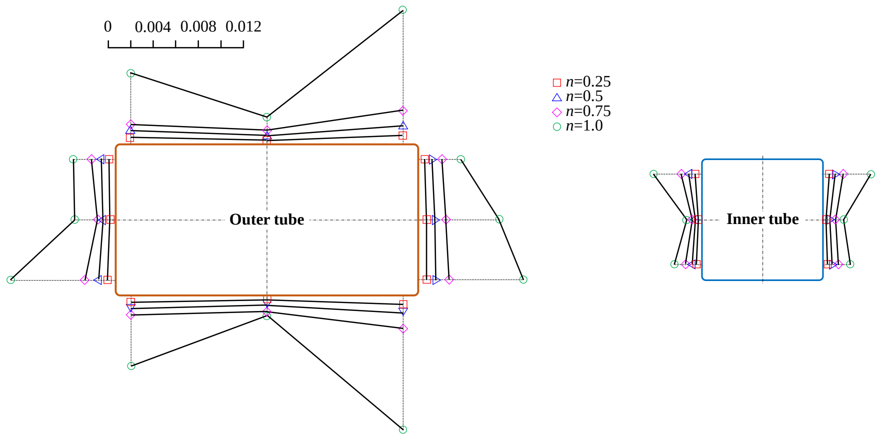

(a) S0.40-57

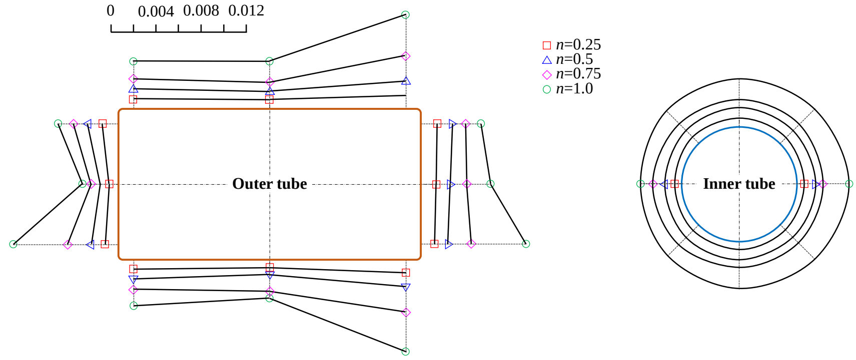

(b) C0.35-48

Fig. 8. Typical longtitudinal strain distribution during the loading process.

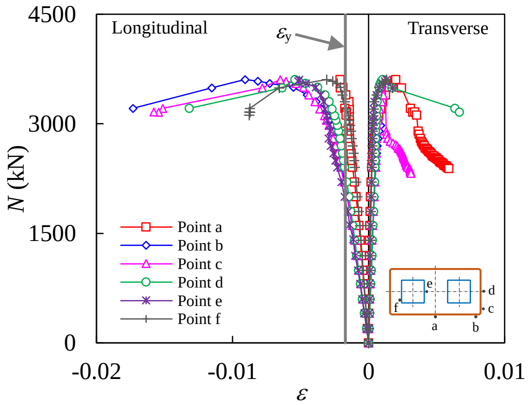

(a) S0.40-57

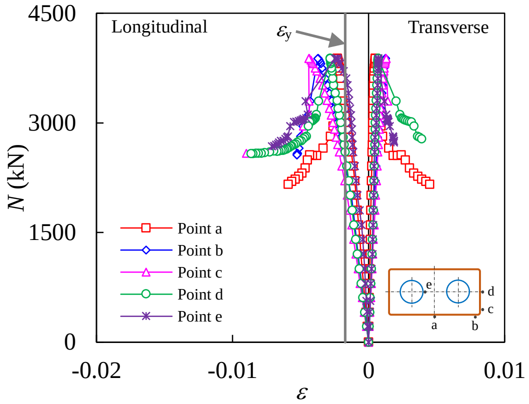

(b) C0.35-48

Fig. 9. Load versus strain curves of typical specimens.

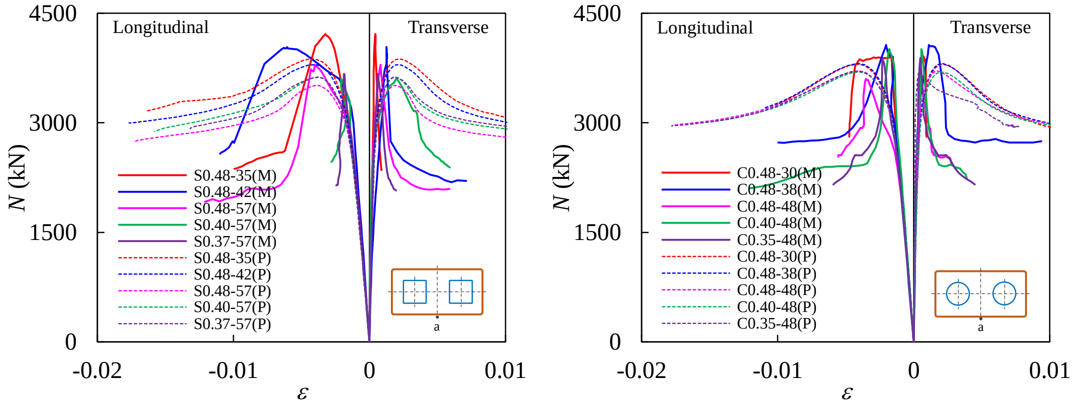

(a) Point a

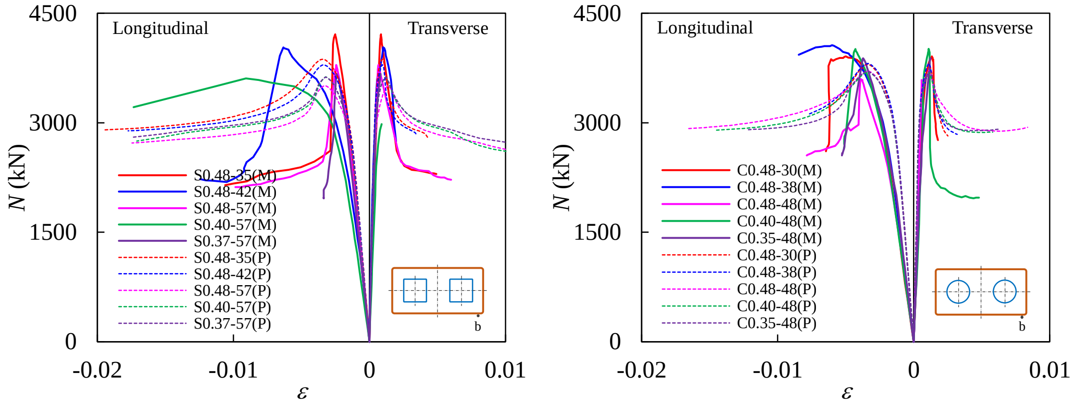

(b) Point b

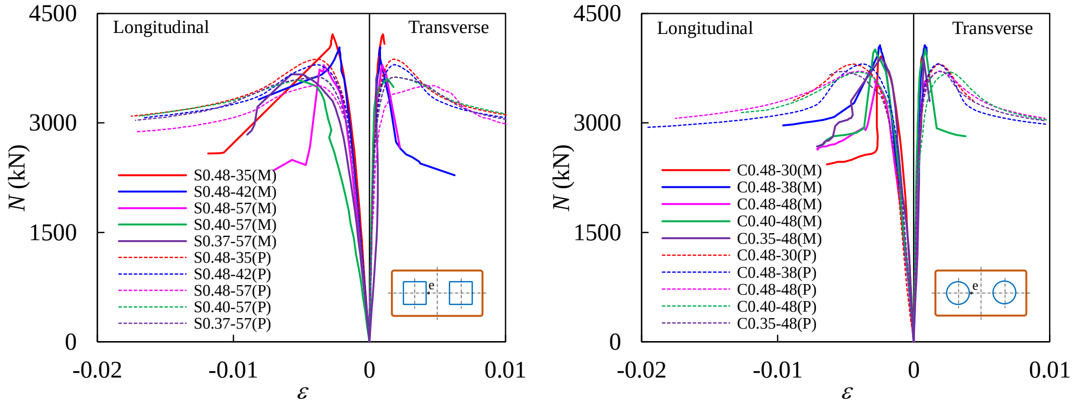

(c) Point e

Fig. 10. Effect of parameters on $N - \varepsilon_{\mathrm{L}}$ curves at representative points.

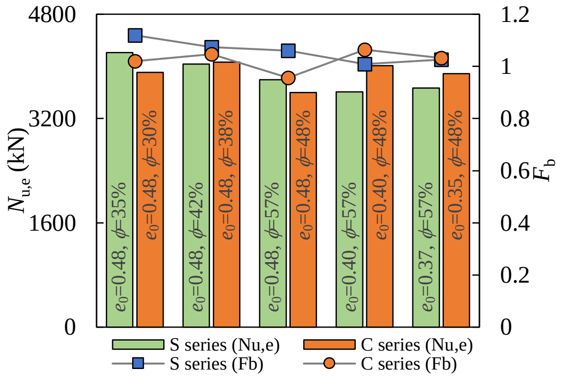

(a) $N_{u,e}$ and F_b

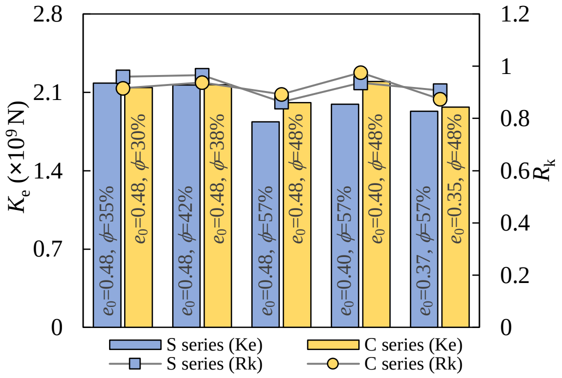

(b) K_e and R_k

Fig. 11. Effect of parameters on $N_{u,e}(F_b)$ and $K_e(R_k)$

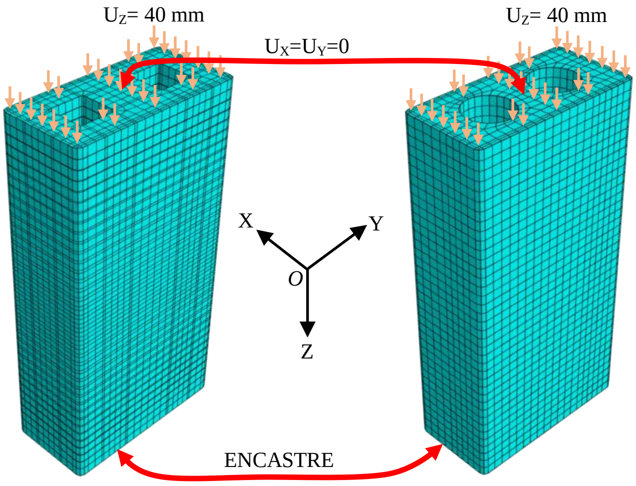

Fig. 12. Meshing and boundary conditions.

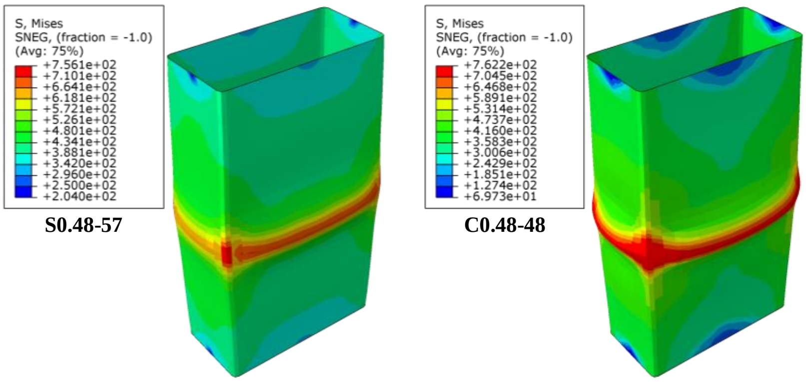

(a) Outer tube

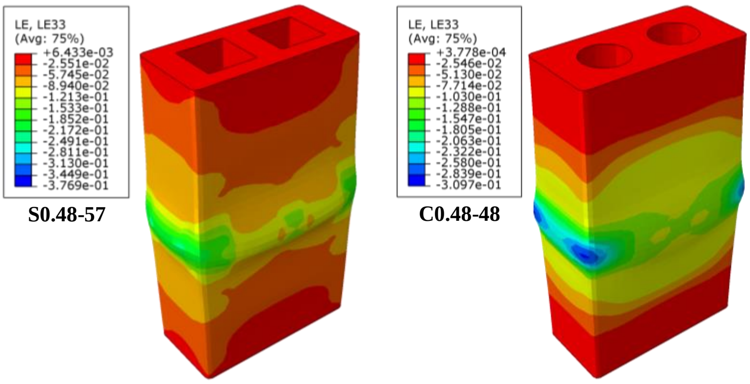

(b) The sandwiched concrete

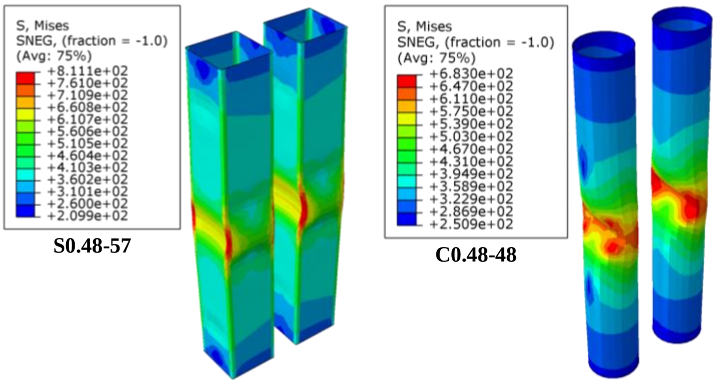

(c) Inner tubes

Fig. 13. The simulated failure mode of different components in typical specimens.

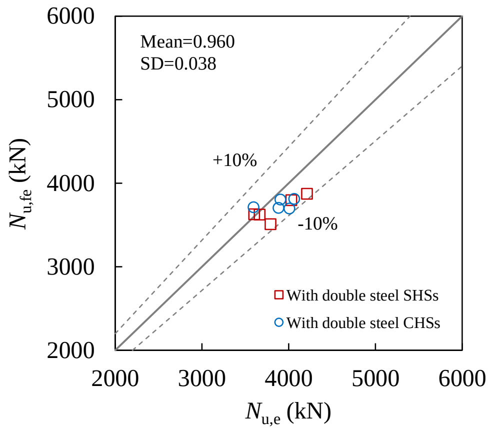

Fig. 14. Comparison between the simulated and measured bearing capacities.

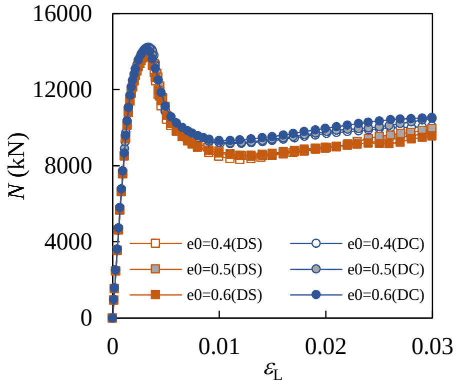

(a) Variation in e_0

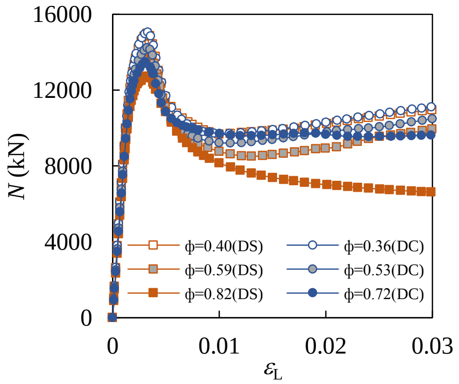

(b) Variation in ϕ

Fig. 15. $N-\varepsilon_{\mathrm{L}}$ curve of typical rectangular DCFSST stub columns under axial compression.

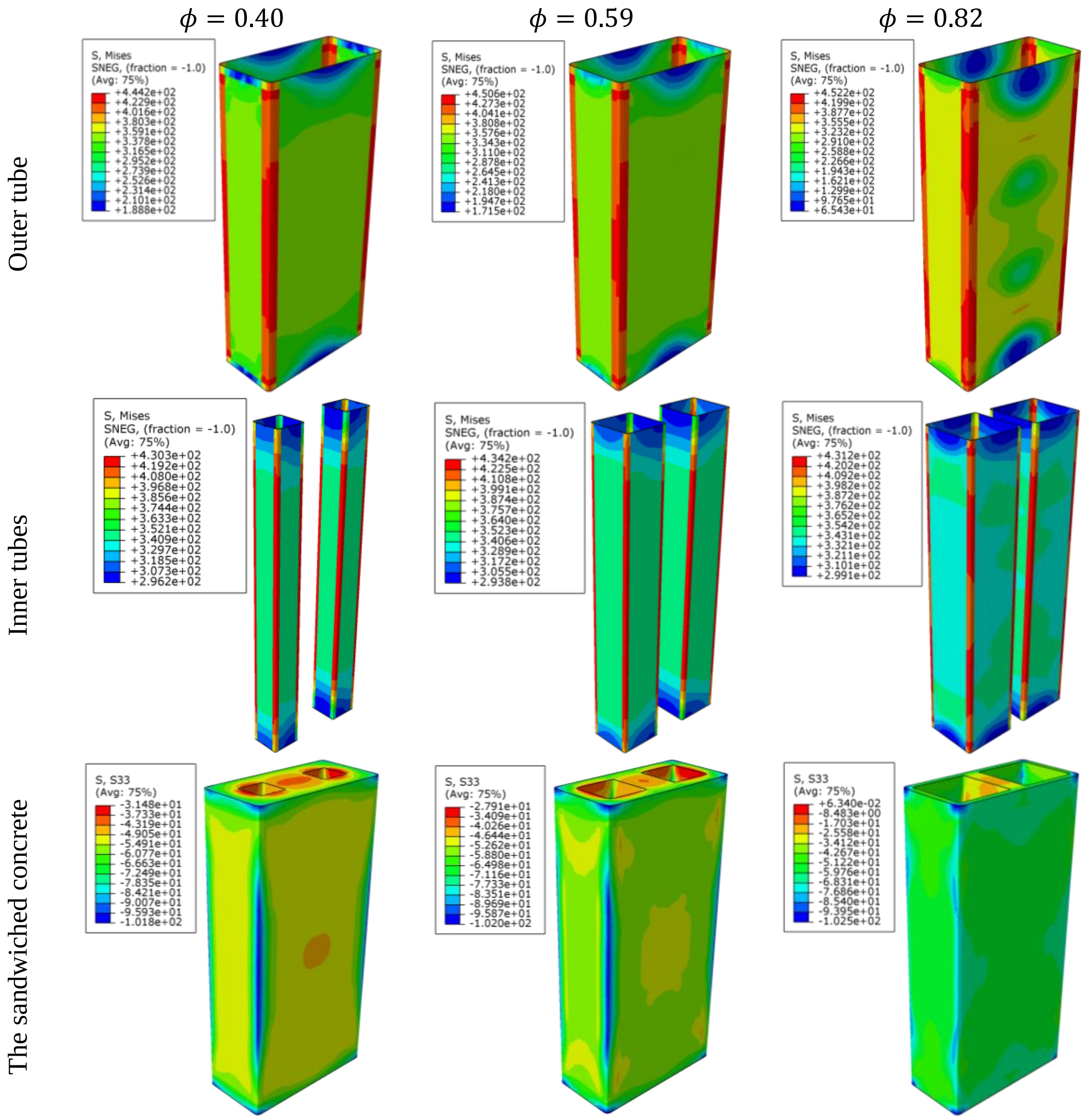

(a) Columns with double steel SHSs

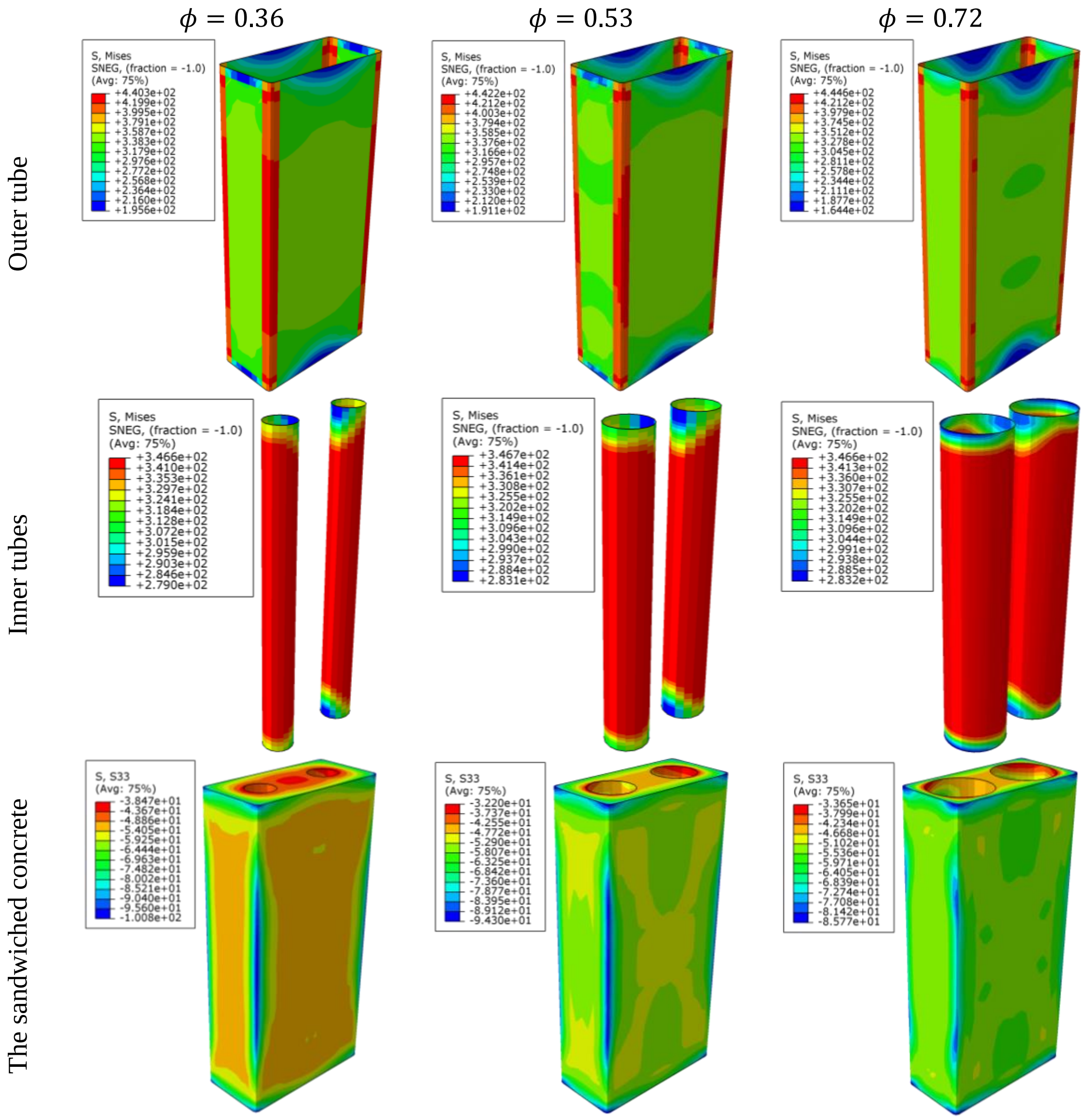

(b) Columns with double steel CHSs

Fig. 16. Effect of ϕ on stress state of different components in the axially compressed rectangular DCFSST stub columns while reaching the bearing capacity.

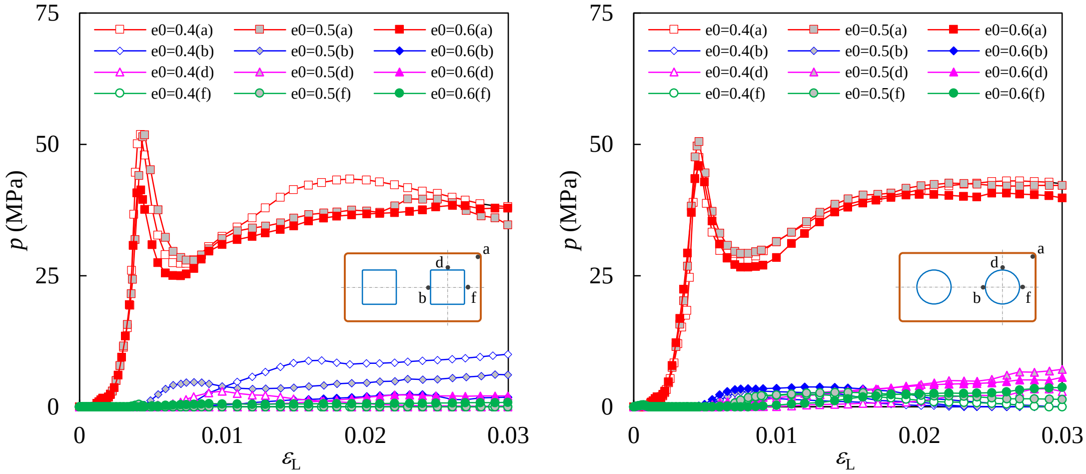

(a) Variation in e_0

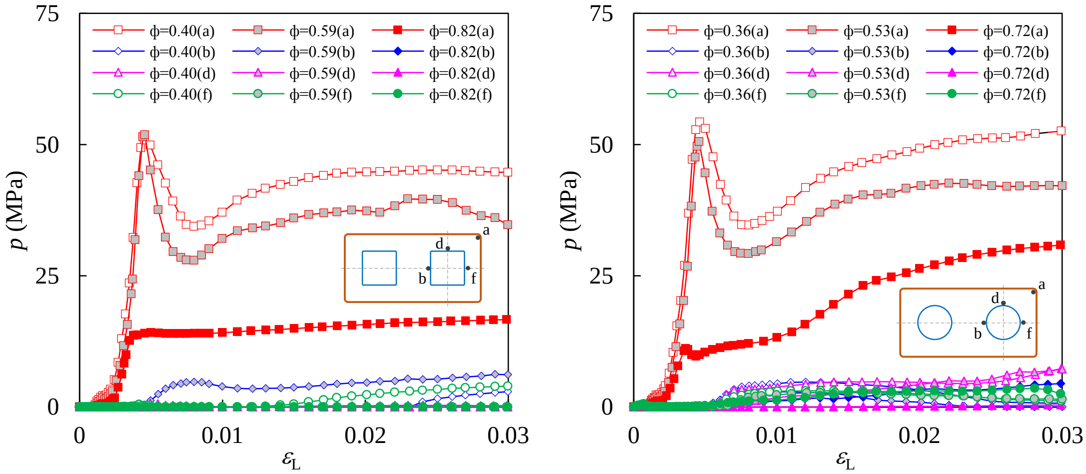

(b) Variation in ϕ

Fig. 17. Effect of e_0 and ϕ on interaction stress between steel tube and concrete.

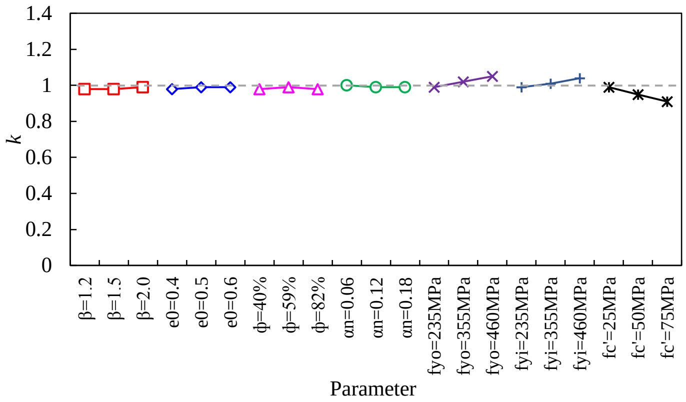

(a) With double steel SHSs

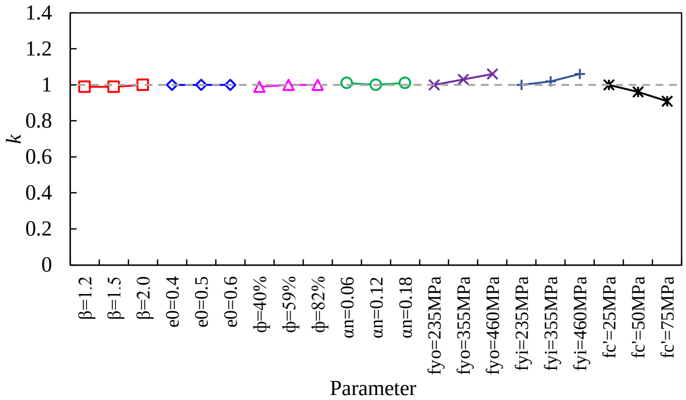

(b) With double steel CHSs

Fig. 18. Effect of parameters on the strength index ratio (k)

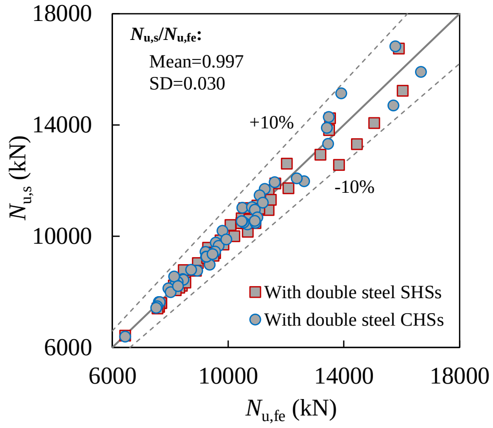

Fig. 19. Comparison between the simplified and numerical bearing capacities.

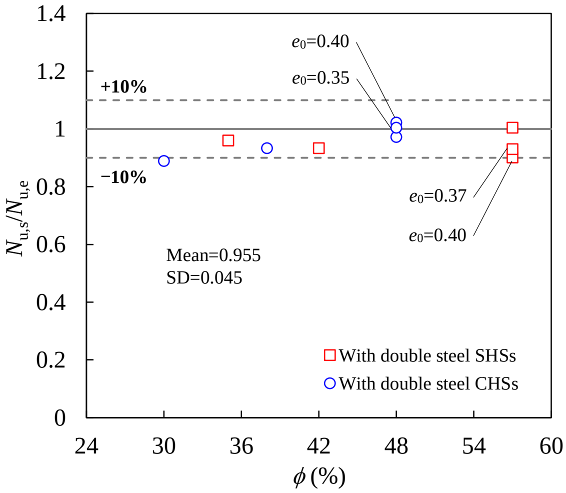

Fig. 20. Comparison between the simplified and measured bearing capacities.

Tables:

Table 1. Information of the test specimens.

No.	Label	$D_o \times B_o \times t_o$ (mm)	D_o/t_o	$D_i \times t_i$ (mm)	D_i/t_i	d_e (mm)	e_0	ϕ	$N_{u,e}$ (kN)	$N_{u,fe}$ (kN)	$N_{u,fe}/N_{u,e}$	K_e ($\times 10^9$N)
1	S0.48-35	300×150×5.65	53.1	50×2.55	19.6	144	0.48	35%	4214	3873	0.919	2.18
2	S0.48-42	300×150×5.65	53.1	60×2.54	23.6	144	0.48	42%	4034	3796	0.941	2.16
3	S0.48-57	300×150×5.65	53.1	80×2.51	31.9	144	0.48	57%	3793	3509	0.925	1.84
4	S0.40-57	300×150×5.65	53.1	80×2.51	31.9	120	0.40	57%	3607	3628	1.006	1.99
5	S0.37-57	300×150×5.65	53.1	80×2.51	31.9	110	0.37	57%	3669	3625	0.988	1.93
6	C0.48-30	300×150×5.65	53.1	48×3.55	13.5	144	0.48	30%	3910	3805	0.973	2.14
7	C0.48-38	300×150×5.65	53.1	60×3.55	16.9	144	0.48	38%	4065	3812	0.938	2.17
8	C0.48-48	300×150×5.65	53.1	76×3.54	21.5	144	0.48	48%	3600	3712	1.031	2.01
9	C0.40-48	300×150×5.65	53.1	76×3.54	21.5	120	0.40	48%	4010	3698	0.922	2.20
10	C0.35-48	300×150×5.65	53.1	76×3.54	21.5	106	0.35	48%	3886	3706	0.954	1.97

Table 2. Properties of steel sections.

Type	Cross-section	$D_o(D_i) \times t_o(t_i)$ (mm×mm)	f_y (MPa)	f_u (MPa)	E_s (N/mm^2)	μ_s	δ (%)
Outer tube	Rectangular	300×5.65	346.5	527.5	2.03×10^5	0.273	30.0
Inner tube	Square	50×2.55	272.8	356.4	1.88×10^5	0.242	15.8
		60×2.54	315.3	407.6	1.85×10^5	0.290	14.3
		80×2.51	303.5	406.2	1.80×10^5	0.268	17.8
	Circular	48×3.55	265.2	348.2	1.99×10^5	0.334	16.0
		60×3.55	329.8	383.4	1.87×10^5	0.277	24.0
		76×3.54	293.6	432.7	1.74×10^5	0.266	28.3

Table 3. Mix proportion and properties of concrete.

Mix proportion (kg/m³)						Properties				
Cement	Fly ash	Sand	Coarse aggregate	Tap water	Water reducer	$f_{cu,28}$ (MPa)	f_{cu} (MPa)	E_c (GPa)	Slump (mm)	Spread (mm)
420	130	800	832	196	5.32	49.4	61.3	31.6	270	600